Oxidation of thin chromium nitride films: kinetics and morphology

1996 J. Phys.: Condens. Matter 8 10703

(http://iopscience.iop.org/0953-8984/8/49/055)

J. Phys.: Condens. Matter **8** (1996) 10703–10719. Printed in the UK

Oxidation of thin chromium nitride films: kinetics and morphology

T Kacsich†, K P Lieb†, A Schaper‡ and O Schulte§

† II. Physikalisches Institut, Universität Göttingen, Bunsenstrasse 7–9, D-37073 Göttingen, Germany

‡ Max Planck Institut für Biophysikalische Chemie, D-37075 Göttingen, Germany

§ I. Physikalisches Institut, Universität Göttingen, D-37073 Göttingen, Germany

Received 15 February 1996

Abstract. Magnetron-sputtered, 150–500 nm thick chromium nitride films of CrN and Cr_2N stoichiometry were exposed to air at 500–800 °C. Oxide scale growth and morphology and the phase transformations during oxidation were investigated by means of Rutherford backscattering spectrometry, resonant nuclear reaction analysis, scanning force microscopy (SFM) and x-ray diffraction. A combined logarithmic and parabolic Cr_2O_3 scale growth was found and interpreted as due to inwards diffusion of oxygen via grain boundaries (logarithmic) and outwards lattice diffusion of Cr (parabolic). Pt-marker experiments confirmed this interpretation. The activation energies of the two processes were determined to be $Q = 60(20)$ and 196(17) kJ mol^{-1}. During oxidation of Cr_2N a transformation into CrN was observed. A linear increase in the surface roughness and surface grain size with the oxide layer thickness was found by SFM.

1. Introduction

Surface finishing by thin film technology is an important industrial process to improve the appearance of materials and to impart properties which deviate from those of the bulk. One example of the improvement of materials like steels and synthetics with respect to their wear and corrosion resistance is the coating with a thin film of metral nitrides [1] such as TiN [2]. Thin films of chromium nitride have aroused technical interest recently [3]. By way of an example, thin CrN films having values of microhardness comparable to those of TiN [4] are easier to deposit by reactive magnetron sputtering, which is a common technique in thin film production: CrN is formed over a larger range of nitrogen partial pressures. This implies a significant simplification in process control [5].

We have recently reported on characteristics like phase formation and surface morphology of magnetron-sputtered chromium nitride films of CrN and Cr_2N stoichiometries as functions of the deposition temperature [6, 7]. In the present study we have extended our investigations of chromium nitride films to their corrosion behaviour after deposition at different substrate temperatures.

Oxidation is influenced by the temperature and the composition of the corroding atmosphere, the stoichiometry of the as-deposited nitride and the morphology of the oxide scale. In the last few years, several investigations on the oxidation of chromium nitrides have been reported in the literature [8–11]. In most of these publications, the oxidation kinetics was considered as a one-dimensional process; that is, only the vertical oxide layer growth and changes in stoichiometry were analysed in terms of their dependences

0953-8984/96/4910703+17$19.50

on oxidation temperature and time. Other parameters that may influence the oxidation behaviour [12], such as the surface morphology and grain structure and the nitride and oxide films, were neglected. In the present study, ion beam analysis methods such as Rutherford backscattering spectrometry (RBS) and resonant nuclear reaction analysys (RNRA) were introduced to monitor the variations in film stoichiometry and oxide layer thickness during oxidation. Although RBS is highly sensitive to the Cr distribution in the samples, depth profiling of the light elements nitrogen (^{15}N) and oxygen (^{18}O) can be performed via RNRA, using the resonant nuclear reactions $^{15}\mathrm{N}(\mathrm{p},\alpha\gamma)^{12}\mathrm{C}$ and $^{18}\mathrm{O}(\mathrm{p},\alpha)^{15}\mathrm{N}$. Compared with more common methods in oxidation science, like thermogravimetry and Auger electron spectrometry, RBS and RNRA are element- and depth-sensitive, non-destructuve methods. Additionally, we applied scanning force microscopy (SFM) and x-ray diffraction (XRD). The high-resolution SFM method enables one to analyse the oxide grain growth, the oxide surface roughness and the density of grain boundaries [13], whereas XRD provides information on the phases and texture of the as-deposited and oxidized films. Only the combination of all these methods led to a comprehensive understanding of the oxidation mechanisms of thin chromium nitride films. We emphasize here that the nanometre resolution of most of the methods employed (SFM, RBS and RNRA) permits the investigation of the early stages of the corrosion process. Samples of CrN and Cr_2N stoichiometry were compared. Insofar as the two nitrides have similar values of the heat of reaction H_R with regard to their transformation into Cr_2O_4 , which is the only stable chromium oxide ($H_R = -885$ kJ mol^{-1} for CrN and -1017 kJ mol^{-1} for Cr_2N [14]), one is interested in the influence of the nitrogen content on the oxidation kinetics. Furthermore, it is often desirable to coat materials at rather low temperatures, for example in the case of polymers. For this reason, we also deposited CrN and Cr_2N films at 20 °C and will compare their oxidation behaviour with that of films deposited at 550 °C substrate temperature.

2. Experimental details

2.1. Preparation of thin films of CrN and Cr_2N stoichiometries and their oxidation

Chromium nitride samples of CrN and Cr_2N stoichiometries were deposited via reactive RF-magnetron sputtering of pure chromium (99.95% purity) in an argon–nitrogen atmosphere onto Si backings of (111) orientation. The deposition temperature was either 20 or 550 °C; the film thickness d_0 was in the range 150–500 nm (see table 1) [6, 7]. The oxidation of these films at temperatures $T_{ox} = 500$–880 °C and in 1 bar air was performed in a commercial furnace. Most samples were isothermally oxidized. Further oxidations of CrN samples in $^{18}O_2$ (98 at% purity, $p = 1$ bar) were performed.

2.2. Rutherford backscattering spectrometry (RBS) and resonant nuclear reaction analysis (RNRA)

The RBS and RNRA analyses were perfomed with the Göttingen 530 kV ion implanted IONAS [15]. RBS is highly sensitive to the chromium concentration profile. The RBS measurements were performed with a 900 keV α-particle beam of 30 nA intensity. A comprehensive description of this method has been given in [16]. The backscattered particles were recorded with two Si surface barrier detectors located at 165° with respect to the incoming beam. The energy resolution of the detectors was 13 keV. The RBS spectra were analysed with the code RUMP89 [17]. Information on the nitrogen profiles of the as-deposited and oxidized samples was obtained by the RNRA method using the resonant

Table 1. Characteristics of the magnetron-sputtered chromium nitride films.

	Deposition temperature T_d (°C)	Chromium concentration (at%)	Phase and texture	Surface grain shape	Surface grain size (lateral diameter D_l) (nm)	Surface roughness R_z (nm)
CrN	20	50(3)	CrN(111)	Spherical	20	15
CrN	550	50(3)	CrN(200)	Tetragonal	35	10
Cr_2N	20	70(3)	Metastable Cr/N	Spherical	20	3
Cr_2N, $d_0 < 250$ nm	550	70(3)	Cr_2N(111)	Spherical	40	5
Cr_2N, $d_0 < 250$ nm	550	70(3)	Cr_2N(110)	Elliptical	$a = 80$ $b = 30$	10

$^{15}N(p, \alpha\gamma)^{12}C$ reaction. The 4.43 MeV γ-ray intensity was measured as a function of the energy of the incident protons. The resonance cross section of this reaction is 300 mbarn, the resonance energy is $E_R = 429.57$ keV and the resonance width (FWHM) is 124 eV [18]. The nitrogen concentration profile was extracted from the γ-ray yield curves, using the exactly known $^{15}N/^{14}N$ isotopic ratio of 3.6×10^{-3} in natural nitrogen. The RNRA yield curves were de-convoluted using the code PRINCE [19] and gave the nitrogen concentration profile $c_N(x)$.

Furthermore, we performed RNRA measurements after oxidation with pure $^{18}O_2$. In this case the nuclear reaction $^{18}O(p, \alpha)^{15}N$ at the 151 keV resonance was used [20]. The 3.2 MeV α-particles from this resonance were detected in a surface barrier detector covered with a 2.5 μm Mylar foil to stop backscattered protons.

2.3. Scanning force microscopy (SFM)

A comprehensive description of the SFM method has been given in [21]. The samples were scanned with a NanoScope III contact SFM (Digital Instruments, Santa Barbara, California, USA). Measurements were performed in air (relative humidity 15–60%) at room temperature (18–27 °C). Imaging was achieved with a J-scanner with a 135 μm(x) $\times$ 135 μm(y) $\times$ 5 μm(z) scan range. We used microfabricated Si tips integrated into triangular cantilevers with typical spring constants of about 0.06 N m^{-1} (Ultralevers, Park Scientific Instruments, Sunnyvale, California, USA). The images were obtained in the topographic mode, which maintains the constant deflection of the cantilever by changing the z extension of the scanner. Images (512×512 pixels) were recorded at a scan frequency of 5 Hz. The image data were processed with the NanoScope software including the operations of plane fitting, flattening and roughness analysis. R_z is the standard deviation of the z values within the selected surface area of typically 2 μm $\times$ 2 μm.

2.4. X-ray diffraction (XRD)

The XRD measurements of the samples were performed with a Philips PW1710 BASED diffractometer in Bragg–Brentano geometry using Cu Kα x-rays. The spectra were accumulated and analysed with the Philips PC-APD 3.5 B code.

3. Results

3.1. Concentration profiles and phase analysis

In table 2, the series of chromium nitride samples after isothermal oxidation in air at T_{ox} are listed, together with their deposition temperature T_d and original layer thickness d_0.

Table 2. The sample treatments.

	Series	d_0 (nm)	T_{ox} (°C)
CrN ($T_d = 20\,^\circ$C)	1	150	500
	2	150	600
	3	150	650
	4	400	650
	5	150	715
	6	250	715
	7	150	750
	8	400	880
Cr_2N ($T_d = 20\,^\circ$C)	1	160	500
	2	180	650
	3	250	650
Cr_2N ($T_d = 550\,^\circ$C)	1	160	500
	2	500	650
	3	160	715
	4	500	715

3.1.1. CrN. The RBS method is highly sensitive to the chromium profile of the samples, whereas the already weak signals from the lighter elements nitrogen and/or oxygen overlap with the backscattered yield from the Si backing. Figure 1(a) illustrates the changes in RBS spectrum of a CrN film ($T_d = 550\,^\circ$C), caused by its oxidation for 2 min at 715 °C. Due to the transformation from CrN to Cr_2O_3, the reduction in the Cr backscattering yield at the high-energy edge, namely at the sample surface, is clearly visible in the RBS spectra. The RNRA spectra of the samples profiled via RBS support this result (see figure 1(b)). Compared with the as-deposited film, the nitrogen profile of the oxidized sample is detected at higher proton energies, for example at larger depths.

Because the chromium, nitrogen and oxygen concentrations add up to unity,

$$c_{Cr}(x) + c_N(x) + c_O(x) = 1 \tag{1}$$

the oxygen concentration $c_O(x)$ and the oxide layer thickness d_{ox} can be calculated. The typical error in d_{ox} is some 4% and illustrates the reliability and precision of the combination of RBS and RNRA. Figure 1(c) illustrates the Cr, N and O concentration profiles of the oxidized CrN sample deduced from the spectra shown in figures 1(a) and (b).

In order to determine the oxygen profile directly (which for oxidation in $^{16}O_2$ was not accessible to us) and to prove the validity of equation (1), we applied the $^{18}O(p,\alpha)^{15}N$ resonance reaction after oxidation of the samples in pure ^{18}O. Figure 1(d) displays the yield N_α of α-particles obtained after a 15 min oxidation of a CrN sample at 715 °C in $^{18}O_2$. The oxygen profile obtained via this measurement is complementary to that obtained indirectly via the RBS/RNRA analyses.

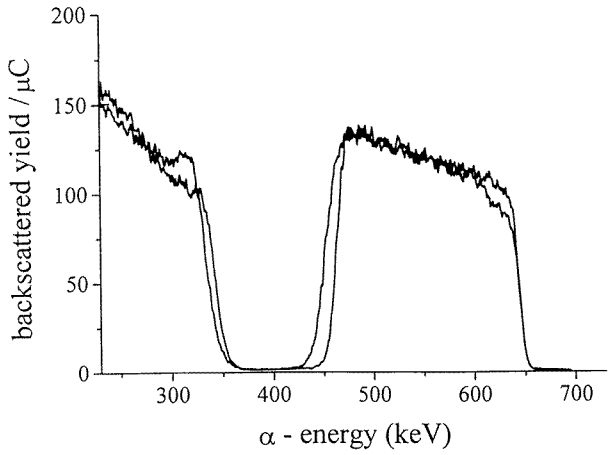

(*a*)

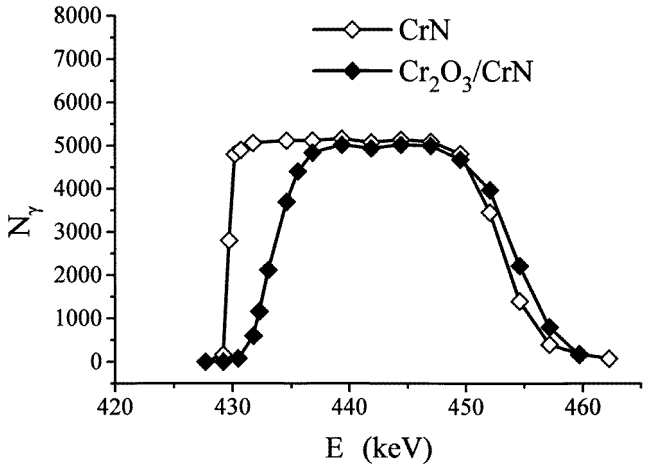

(*b*)

Figure 1. (*a*) RBS spectra of a CrN ($T_d = 550\,^{\circ}$C) sample before and after oxidation for 2 min at 715 °C in air. Both the high-energy tail of the Cr signal and the high-energy tail of the Si signal (oxygen take-up) illustrate the oxidation. (*b*) The RNRA γ-ray yield function of the CrN ($T_d = 550\,^{\circ}$C) sample in (*a*). The Cr_2O_3 layer is illustrated by the shift of the N_γ yield to larger energies in the oxidized sample, which is in contrast to the case of the as-deposited sample. (*c*) Concentration profiles of the elements Cr, N and O in the oxidized CrN ($T_d = 550\,^{\circ}$C) sample of (*a*) and (*b*). (*d*) The N_α yield of the $^{18}O_2(p,\alpha)^{15}N$ resonant reaction of a CrN ($T_d = 550\,^{\circ}$C) sample subsequently oxidized at 715 °C for 15 min in pure $^{18}O_2$ (open symbols) and for 15 min in air (filled symbols).

In figure 2(*a*) the XRD pattern of the RBS and RNRA profiled CrN 550 °C sample is compared with that of the as-deposited one. Besides the CrN (111) and (110) peaks, the Cr_2O_3 (100) and (113) reflections are visible in the spectrum, whereas the strong (104) peak of polycrystalline Cr_2O_3 powder is absent, indicating a pronounced texture of Cr_2O_3. It can be seen in figure 3 that the overall amount of nitrogen in the sample is reduced during oxidation.

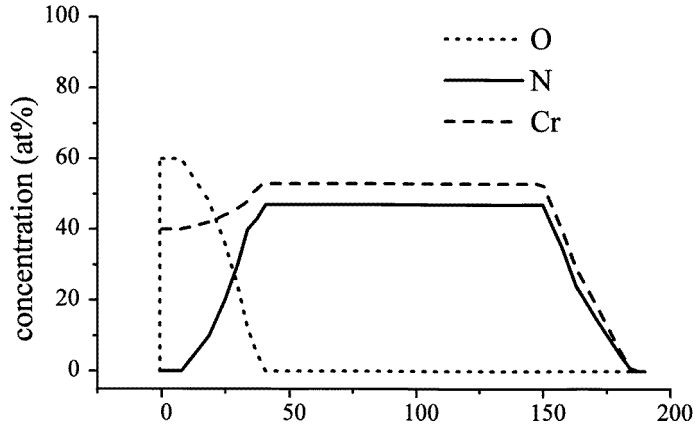

(*c*)

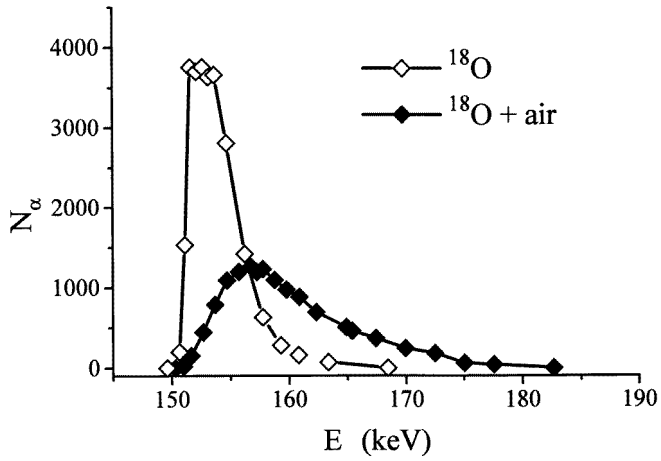

(*d*)

Figure 1. (Continued)

CrN samples deposited at 20 °C failed during oxidation above 600 °C due to crack formation and pealing off from the silicon backing. This was not observed for the CrN samples deposited at 550 °C. The CrN 20 and 550 °C films were both formed in the thermodynamically stable CrN phase, but with different textures: CrN (111) at 20 °C and CrN (11) at 550 °C. This indicates a correlation between the texture and the adhesion to the Si substrate after oxidation. Moreover, one can conclude that the failure of the CrN room temperature (RT) films is not correlated to thermal stresses between the nitride and the silicon backing, but rather to growth stresses during oxide formation. This assumption is supported by the fact that, when the CrN RT films were heated in vacuum without any oxidation, they revealed neither crack formation nor pealing off from the substrate. Stresses caused by different volume expansions of the oxide and of the thin films [22] or stresses enhanced by an oxidation process, in which grain boundary and volume diffusion occur simultaneously [23], have been discussed in the literature. In the present case, one has to take into account that an oxide layer texture caused by a quasi-epitaxial film growth implies

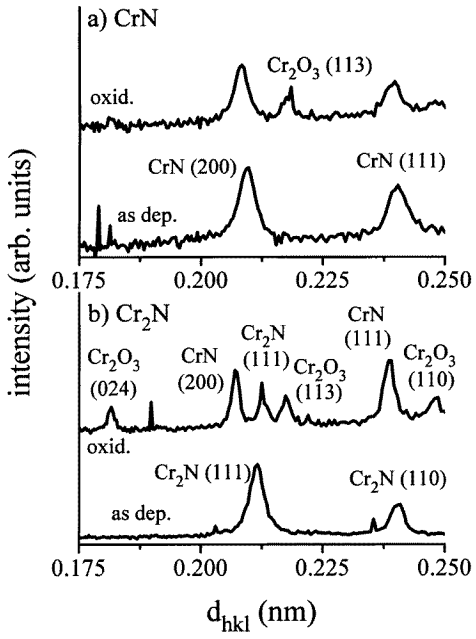

Figure 2. (*a*) XRD spectra of a CrN sample ($T_d = 550\,^{\circ}$C), as deposited and oxidized in air for 2 min at 715 °C. (*b*) The same but for a Cr_2N ($T_d = 550\,^{\circ}$C) sample. Note the CrN reflections in the pattern of the oxidized sample.

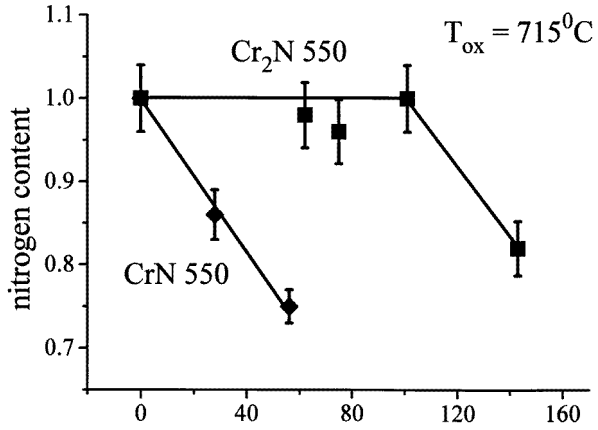

Figure 3. The overall nitrogen content of a CrN sample (*a*) and of a Cr_2N sample (*b*) as a function of the oxide layer thickness.

crystalline mismatch and growth stresses between oxide and nitride. This phenomenon has been investigated in detail in [24, 25]. It is in line with these latter studies that our XRD measurements yielded differently textured oxide layers grown on CrN 550 °C, Cr_2N 20 °C and Cr_2N 550 °C samples.

3.1.2. Cr_2N. In contrast to the CrN RT films, no cracks were observed for Cr_2N 20 °C and Cr_2N 550 °C samples during oxidation. The XRD pattern of an oxidized Cr_2N 550 °C sample shown in figure 2(*b*) revealed, besides the (113) peak of the textured Cr_2O_3 layer and the original Cr_2N peaks, the (111) and (200) peaks of the CrN phase. This additional nitridization of Cr_2N during the oxidation was also clearly visible in the concentration profiles of this sample, which were obtained via RBS and RNRA and are plotted in figure 4. The surface oxide scale is followed by a layer of enhanced nitrogen content compared with that of the as-deposited Cr_2N stoichiometry, which is still present at larger depths. During continued oxidation, that Cr_2N to CrN transformation affects the whole of the remaining nitride layer. The total nitrogen content in the nitride layer during oxidation is constant until the oxide layer has reached a thickness of approximately 40–60% of the as-deposited Cr_2N layer (see figure 3(*b*)). In contrast to the case of CrN, the Cr_2N acts as a buffer for the nitrogen content of the nitride and transforms into CrN. As soon as all Cr_2N has transformed into Cr_2O_3 and CrN, the nitrogen has to diffuse out of the sample and the overall nitrogen content starts to decrease. This competition between (outer) oxidation and (inner) nitridization has been reported previously [5, 26].

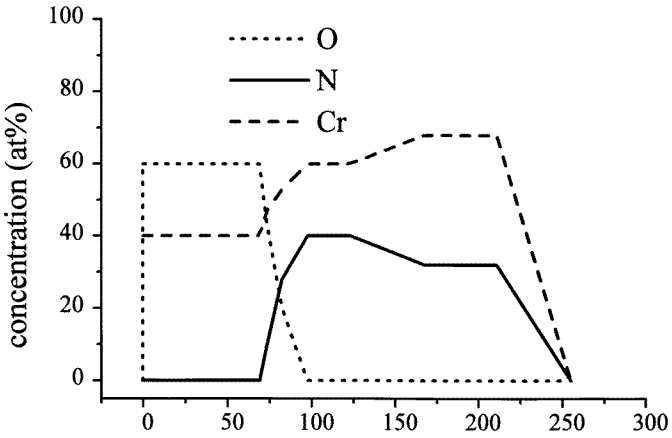

Figure 4. Concentration profiles of Cr, O and N for a Cr_2N ($T_d = 550$ °C) sample oxidized in air for 1 min at 715 °C.

The oxidation of the Cr_2N RT samples follows the same scheme. The oxide layers are (104) textured, in contrast to the Cr_2N 550 °C samples, for which the oxide is (113) textured, irrespective of the original Cr_2N thickness. The influence of the inner nitridization on the proceeding of the oxide scale growth during the isothermal oxidation of Cr_2N at 650 °C is visible in figure 5: here the oxide layer thickness d_{ox} is plotted as a function of the oxidation time for Cr_2N 20 °C samples, originally 160 and 250 nm thick, and for a CrN 550 °C sample. We first note that the oxidation of Cr_2N proceeds faster than does that of CrN. For the 160 nm Cr_2N 20 °C samples, the oxidation changes at an oxide layer thickness of about 80 nm from that typical of Cr_2N to that typical of CrN.

3.2. Oxide surface topography

All the SFM pictures were analysed to obtain their mean roughness parameter R_Z and the area A of the surface grains in terms of their dependences on the oxide layer thickness. Figure 6 displays two SFM scans of a Cr_2N 20 °C sample covered with 40 and 160 nm

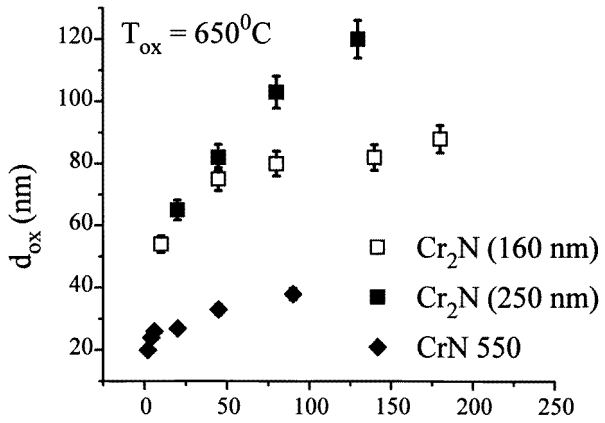

Figure 5. Isothermal oxidation of Cr_2N ($T_d = 20\,^{\circ}C$) samples ($d_0 = 160$ and 250 nm) and of a CrN ($T_d = 550\,^{\circ}C$) sample ($d_0 = 400$ nm) at 650 °C. Note the change in slope for the 160 nm Cr_2N ($T_d = 20\,^{\circ}C$) sample due to the $Cr_2N \rightarrow$ CrN transformation, which has gone to completion. For details see the text.

oxide layers. The surface exhibited a granular structure. In figure 6(*a*) the mean surface grain area is 24 000 nm^2; in figure 6(*b*) it is 80 000 nm^2. For all the investigated samples, the values of R_z and A correlated linearly with the oxide layer thickness (see table 3), independently from the initial nitride phase and stoichiometry.

Table 3. The oxide scale d_{ox}, surface roughness R_Z and grain area A of oxidized samples.

Sample	d_{ox} (nm)	R_Z (nm)	A (10^2 nm^2)
CrN ($T_d = 550\,^{\circ}C$) 5,8	20	11(2)	45(7)
	26	14(2)	68(10)
	27	17(3)	88(13)
	34	17(3)	120(18)
	41	17(3)	150(23)
	60	20(3)	320(48)
	80	34(5)	400(60)
	116	37(6)	520(78)
Cr_2N ($T_d = 20\,^{\circ}C$) 3	40	20(3)	240(36)
	66	30(5)	320(48)
	86	41(6)	470(70)
	160	74(11)	800(120)
Cr_2N ($T_d = 550\,^{\circ}C$) 2	80	34(5)	510(77)
	114	51(8)	620(93)
	125	70(11)	590(88)
	160	95(14)	660(100)

At this point we have to discuss the correlation between the average surface roughness R_z and the apparent thickness variance $\Delta d = 2\sigma$ of the oxide/nitride interface obtained from the nitrogen concentration profiles at the interface determined by RBS and RNRA. Both methods are sensitive to the concentration profiles convoluted with the energy loss of the protons or the α-particles in the sample. The RUMP89 and PRINCE codes fit the

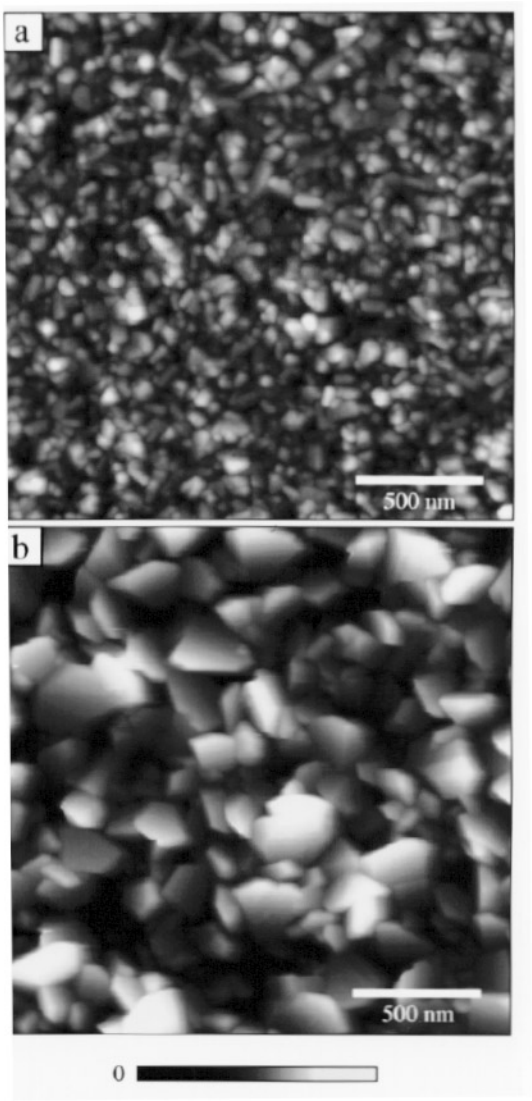

Figure 6. SFM measurements of Cr_2O_3 surface layers on Cr_2N ($T_d = 20\,^{\circ}C$) samples: (*a*) $d_{ox} = 40$ nm and (*b*) $d_{ox} = 160$ nm.

experimental data, assuming a homogeneous lateral energy loss of the particles. This does not hold in the case of a structured surface or interface. Several limiting cases are sketched in figure 7. Assuming a sharp interface and a structured surface, R_Z and Δd would be equal (figure 7(*a*)). The opposite case of a flat surface and an interface broadened by grain structure (figure 7(*b*)) or pure interdiffusion (figure 7(*c*)) would lead to $R_Z \ll \Delta d$. If the surface and interface morphology were to follow each other, as displayed in figure 7(*d*), the top layer thickness would stay essentially constant while the surface roughness could be large: $R_Z \gg \Delta d$. Yet another case occurs (figure 7(*e*)) when a rough surface and a rough interface are uncorrelated, leading to high R_Z and still higher $\Delta d > R_Z$. A comparison of the two parameters R_Z and Δd therefore allows one to characterize both the surface and

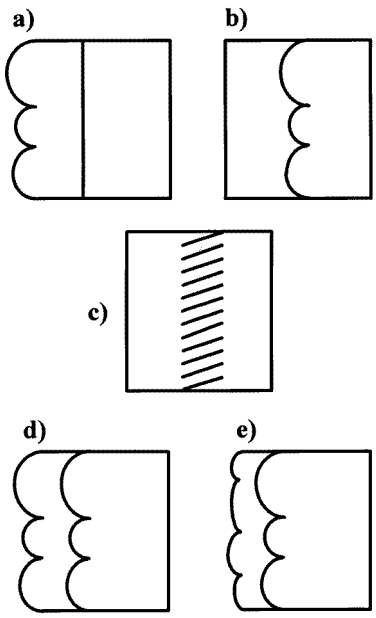

Figure 7. Qualitative interpretations of the oxidation of chromium nitride samples. For details see the text.

the interface morphology, whereas neither SFM nor RBS/RNRA alone would simply give unambiguous information on these important quantities.

In figure 8, the R_Z values obtained from SFM and the apparent widths Δd deduced from RBS and RNRA are plotted versus the Cr_2O_3 layer thickness. It was found that, for the Cr_2N 550 °C samples, the Δd values were almost constant and smaller than the R_Z values. This means that the oxide/nitride interface essentially follows the surface morphology (the case shown in figure 7(*d*)). However, the Δd values for CrN increased during oxidation and were larger than the R_Z values. This means that the oxidation seems to lead to the situation pictured in figure 7(*e*). Nevertheless, with knowledge of the diffusion of nitrogen outwards during the oxidation of CrN (figure 3), a mixture of figures 7(*b*) and (*d*) gives the most appropriate interpretation of the data: during the oxidation of CrN, the surface and the interface structure follow each other (figure 7(*d*)), whereas the enlargement of Δd with respect to the R_Z values is due to the diffusion of nitrogen outwards (figure 7(*b*)).

In the following, we adopt a model of oxide scale growth based on the work of Kofstad on the oxidation of pure chromium [12]. The oxidation process of chromium nitride layers is dominated by two different processes: on the one hand, the outwards volume diffusion of Cr through the oxide scale and, on the other hand, the diffusion of oxygen inwards through the oxide grain boundaries. The oxide scale growth occurs simultaneously at the oxide surface, the oxide grain boundaries and the oxide/nitride interface. During oxidation, the lateral oxide grain size increases. If both processes contribute to the oxide growth, a lateral homogeneous oxide layer will be formed, leading to the same values of the surface roughness and the interface width.

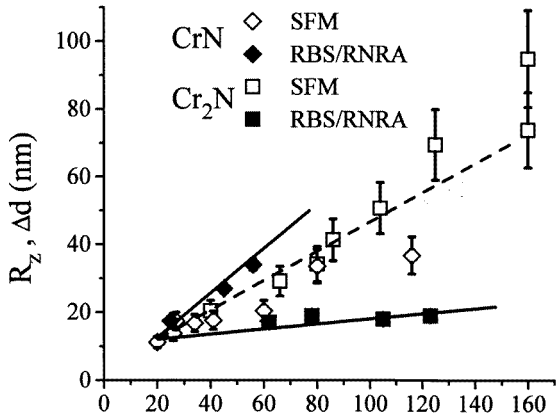

Figure 8. The surface roughness (R_Z) and apparent oxide layer thickness variation (Δd) of oxidized CrN and Cr_2N samples versus the oxide layer thickness d_{ox}.

3.3. Marker experiments

In order to test whether oxygen diffuses inwards while chromium diffuses outwards through the oxide scale, we have performed a marker experiment in such a way that a 0.5 nm thick Pt marker was deposited on top of a Cr_2N 550 °C layer via electron beam evaporation. The sample was then heated twice in air at 715 °C for 1 min each time. After each oxidation step, an RBS spectrum was recorded (figure 9(*a*)), leading to the Pt concentration profiles shown in figure 9(*b*). The oxide layer thicknesses after each oxidation (57(5) nm after 1 min, 78(6) nm after 2 min) are within the error the same as those for samples oxidized without the Pt marker. If now the oxidation proceeds only by diffusion outwards of Cr, one would expect the Pt marker after oxidation to be right at the oxide/nitride interface. If, on the other hand, the oxidation were controlled exclusively by diffusion inwards of oxygen, the Pt marker would remain at the surface of the sample. The experimentally determined locations of the Pt marker, 41(3) nm after 1 min and 58(4) nm after 2 min, clearly prove that both diffusion processes occur. In this context, we mention the ^{18}O profiles measured after two subsequent oxidations at 715 °C, first in pure $^{18}O_2$ (open symbols) and then in air (filled symbols), shown in figure 1(*d*). The $^{18}O_2$ distribution after the exposure to pure $^{18}O_2$ does not stay constant during the second oxidation in air. The onset of the resonance moves to larger proton energies, namely a larger layer depth, while the integrated yield is reduced by 25%. This is a consequence of the diffusion mechanisms enhanced by the oxidation, but also of an $^{18}O_2 \leftrightarrow {}^{16}O$ exchange within the Cr_2O_3 layer. For that reason, this experiment, although consistent with the results obtained via the Pt marker experiment, cannot unambiguously prove them.

3.4. Oxidation kinetics

In the literature many oxidation models have been reported which correlate the oxide scale growth with the oxidation temperature T_{ox}, the time of oxidation and various structural and thermodynamical properties.The common integrated rate equations describing the oxide layer growth are the logarithmic rate equation

$$d_{ox} = k_l \ln(t/t_0 + 1) + A \tag{2}$$

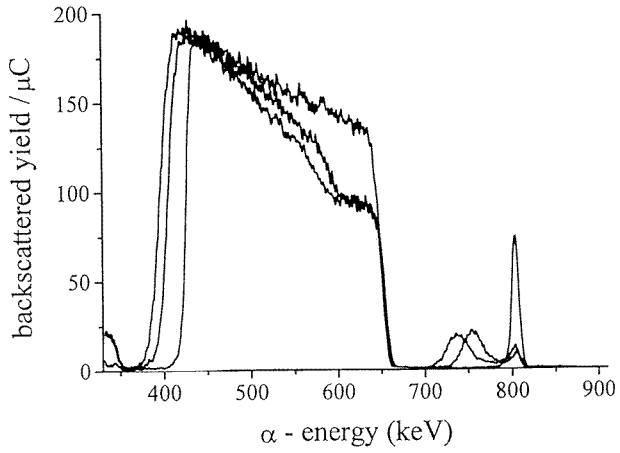

(*a*)

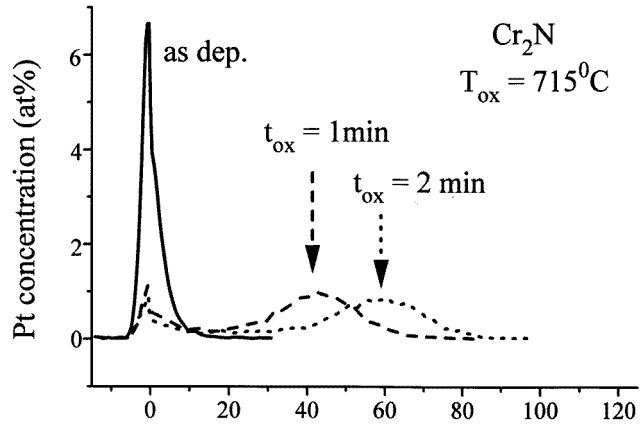

(*b*)

Figure 9. (*a*) RBS spectra of a Cr_2N ($T_d = 550\,^{\circ}C$) sample covered with a Pt marker layer, recorded in the as-deposited state and after oxidation for 1 and 2 min in air at 715 °C. (*b*) Pt concentrations extracted from the spectra shown in (*a*).

and the parabolic rate equation

$$d_{ox}^2 = k_p t + B. \tag{3}$$

The logarithmic rate equation applies, for example, to situations in which the rate-dominating process is the tunnelling of electrons through the oxide layer [27] or, as described in the model of Davies *et al* [28], the diffusion of oxygen at grain boundaries. The model of Davies *et al* is based on the assumption that the oxide grain scale growth occurs simultaneously at the oxide/material interface and at the oxide grain boundaries; that is, both the thickness and the vertical grain size are increasing, while the number of diffusion paths in the grain boundaries is decreasing. The parabolic rate equation formulated by Wagner [29] for the oxidation of metals is based on Fick's law of metal or oxygen volume diffusion through the oxide layer driven by the gradient of the electrochemical potentials.

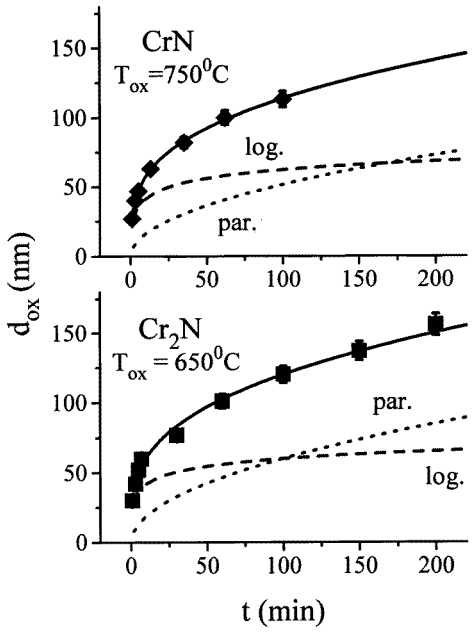

Figure 10. Isothermal oxidation of CrN samples at 750 °C (*a*) and of Cr_2N samples at 650 °C (*b*). The fit to the oxide layer thickness d_{ox} follows a combined rate equation with the logarithmic and parabolic contributions shown.

For constant oxygen partial pressure, the temperature-dependence of the logarithmic and the parabolic rate constants follows an Arrhénius law:

$$k = k_0 \exp[-Q/(RT_{ox})] \tag{4}$$

where Q signifies the activation energy of the oxidation process.

As mentioned in section 3.1, the isothermal oxidation of Cr_2N 550 °C samples at T_{ox} = 500–880 °C proceeds faster than does that for CrN 550 °C samples. In both films, the oxide scale growth was found to follow neither the logarithmic nor the parabolic rate equation. However, a good description of the data was achieved with a combination of the two rate constants (see figure 10):

$$d_{ox} = k_l \ln(t/t_0 + 1) + (k_p t)^{0.5}. \tag{5}$$

Based on the results of the SFM and RBS marker experiments, we interpret the logarithmic term as being due to grain boundary diffusion inwards of oxygen and the parabolic term as being due to volume diffusion of chromium outwards. We further note that the two diffusion processes in this model do not interact with each other and start without any measurable offset in oxide layer thickness. The oxygen grain boundary diffusion dominates the oxidation of thin nitride films, which have small grains and a large amount of grain boundaries. In contrast, chromium volume diffusion (outwards) is the rate-determining process for larger oxide scale thicknesses, large grain sizes and a correspondingly small amount of grain boundaries. Using $\lambda = 0.5$ nm for the width of the grain boundaries [30], the parameter $f = 3\lambda/A$ relates to the oxide grain area A obtained via SFM. Indeed, it can be seen in figure 11, that f decreases for increasing oxide layer thickness.

From the Arrhénius plots of k_l and k_p shown in figures 12(*a*) and (*b*), the activation energies Q_l and Q_p were determined for both nitrides (see table 4). The Q_l and Q_p values

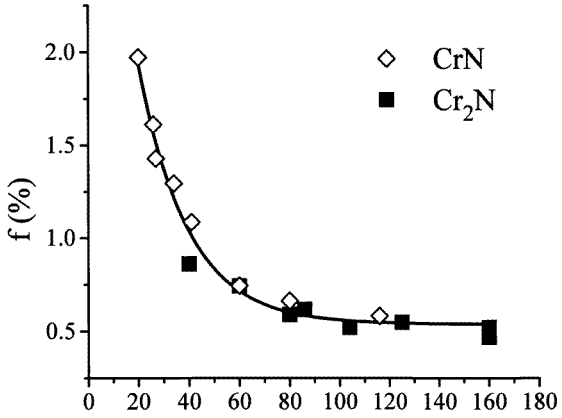

Figure 11. The fraction of grain boundaries f as a function of the oxide layer thickness.

agree, within the errors, for both nitride phases. The mean values deduced from all the data are $Q_l = 60(20)$ kJ mol^{-1} and $Q_p = 196(17)$ kJ mol^{-1}. These facts indicate that the diffusion of nitrogen outwards, which occurs only for the CrN samples, is not the rate-determining diffusion process of the oxidation. Nevertheless, the faster isothermal oxidation of Cr_2N compared with that of CrN, is due to the influence of the nitrogen. Assuming that the Cr volume diffusion outwards is controlled by an interstitial diffusion mechanism, k_p is proportional to the chromium activity a^i_{Cr} at the oxide/nitride interface, where we have used $k_p = D^V_{Cr}a^i_{Cr}$ with D^V_{Cr} denoting the volume diffusion constant [29]. This activity is larger for Cr_2N than for CrN: in the case of Cr_2N, nitrogen diffuses into larger nitride layer depths and initiates the inner nitridization of Cr_2N.Therefore, the oxidation rate for Cr_2N is larger than that for CrN.

Table 4. Activation energies for logarithmic and parabolic rate equations.

	Q_l (kJ mol^{-1})	Q_p (kJ mol^{-1})
CrN ($T_d = 550\,^\circ$C)	69(16)	51(24)
Cr_2N ($T_d = 550\,^\circ$C)	188(14)	204(20)

In contrast to the present results, parabolic oxidation of chromium nitride films has been described in the literature for the same range of oxidation temperatures as in our experiments [9, 11, 31]. Activation energies of 150 [9] and 123 kJ mol^{-1} [11] for the oxidation of CrN, and 123 kJ mol^{-1} for Cr_2N [31], were reported and Cr volume diffusion was noted to be the rate-determining process. In these studies, the authors extracted the activation energies via AES depth profiling and without any investigation of the oxide surface topography using $d_{ox} \sim \exp[-Q/(2RT)]$. This equation only holds if the oxidation starts without any offset according to $d^2 = k_p t$.

4. Summary

In this work, the oxidation of magnetron-sputtered chromium nitride films of CrN and Cr_2N stoichiometry was investigated via a combination of the high-resolution methods

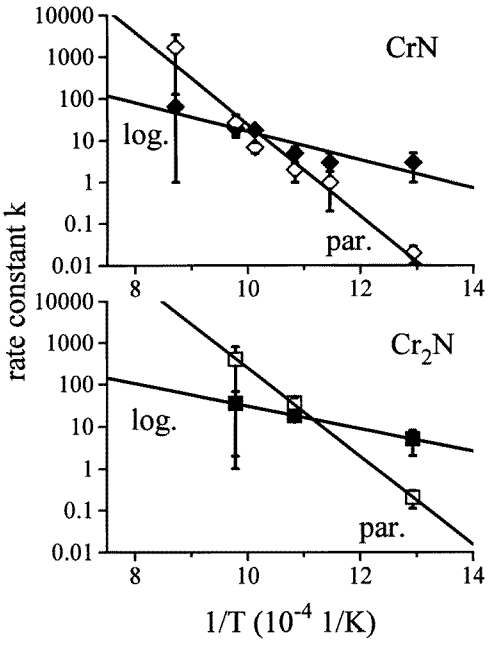

Figure 12. Arrhénius plots of the rate constants k for the oxidation of CrN (*a*) and Cr_2N (*b*).

RBS, RNRA, SFM and XRD. Whereas the ion beam methods measure the oxidation-induced changes in concentration profiles, the SFM method gives access to the oxide surface topography. Additional information on phase formation during the oxidation was extracted from XRD We emphasize again that the combination of RBS, RNRA and SFM was very important to separate the effects of the rough oxide surface and the rough oxide/nitride interface. Furthermore, marker experiments with a thin Pt marker clarified important details of the oxidation mechanism.

On the basis of the results obtained via these methods, we were able to model the oxidation of chromium nitride layers in detail. In both types of samples, the isothermal oxidation at 500–880 °C follows a combined logarithmic/parabolic rate equation. The grain boundary diffusion of oxygen inwards (logarithmic contribution) dominates the oxidation process at small oxide layer thicknesses, namely for small oxide grain sizes and a large amount of grain boundaries. The volume diffusion of chromium outwards (logarithmic contribution) is the rate-dominating process for large oxide layer thicknesses. Indications of the influence of growth stresses on the oxidation were found. Additional *in situ* stress measurements have to be performed.

Acknowledgments

The authors would like to thank D Purschke for expertly operating the IONAS accelerator and Professor H G Wagner for advice. This work was supported by the Deutsche Forschungsgemeinschaft (DFG Li325).

References

[1] Frey H and Kienel G (eds) 1987 *Dünnschichttechnologie* (Düsseldorf: VDI)
[2] Sundgren J-E, Johansson B-O and Karlsson S-E 1983 *Thin Solid Films* **105** 353
[3] Chang Y G, Warsop R K, Farb N E and Parson R 1994 *Surf. Coating Technol.* **68/69** 157
[4] Münz W D and Göbel J 1987 *Surf. Eng.* **3** 47
[5] Knotek O, Bosch W, Atzor M, Münz W-D, Hoffmann D and Göbel J 1986 *High Temp. High Press.* **18** 435
[6] Kacsich T, Neubauer M, Geyer U, Baumann K, Rose F and Uhrmacher M 1995 *J. Phys. D: Appl. Phys.* **28** 424
[7] Kacsich T, Niederdrenk M, Schaaf P, Lieb K P, Geyer U and Schulte O 1996 *Mater. Sci. Res.* at press
[8] Schröer A, Ensinger W and Wolf G K 1991 *Mater.Sci. Eng.* A **140** 625
[9] Hofmann S and Jehn H A 1990 *Werkstoffe Korrosion* **41** 756
[10] Knotek O, Löffler F and Scholl H-J 1991 *Surf. Coating Technol.* **45** 53
[11] Huber E and Hofmann S 1994 *Vacuum* **45** 1003
[12] Kofstad P 1988 *High Temperature Corrosion* (New York: Elsevier)
[13] Ocon P, Herrasti P, Vazques L, Salvarezza R C, Vera J M and Arvia A J 1991 *J. Electroanal. Chem.* **319** 101
[14] 1982–3 *CRC Handbook of Chemistry and Physics* 63d edition (Boca Raton, FL: CRC Press)
[15] Uhrmacher M, Pampus K, Bergmeister F J, Purschke D and Lieb K P 1985 *Nucl. Instrum. Methods* B**9** 234
[16] Chu W K, Mayer J W and Nicolet M A 1987 *Backscattering Spectrometry* (New York: Academic)
[17] Doolittle L R 1985 *Nucl. Instrum. Methods* B **9** 344
[18] Osipowicz T, Lieb K P and Brüssermann S 1987 *Nucl. Instrum. Methods* B **18** 232
[19] Borowski M, Illgner C and Kacsich T unpublished
[20] Borowski M 1992 *Diplomarbeit* Universität Göttingen
[21] Sarid D 1991 *Scanning Force Microscopy* (Oxford: Oxford University Press)
[22] Pilling N B and Bedworth R E 1923 *J. Instrum. Methods* **29** 529
[23] Kofstad P and Lillerud K P 1980 *J. Electrochem. Soc.* **127** 2410
[24] Borie B S, Sparks C J and Cathcart J V 1962 *Acta. Metall.* **5** 691
[25] Cathcart J V and Peterson G F 1968 *J. Electrochem. Soc.* **115** 595
[26] Kacsich T and Lieb K P 1994 *Thin Solid Films Lett.* **235** 4
[27] Mott N F 1947 *Trans. Faraday Soc.* **43** 429
[28] Davies D E, Evans U R and Agar J N 1954 *Proc. R. Soc.* A **225** 443
[29] Wagner C 1933 *Z. Phys. Chem.* B **21** 25
[30] Böhm H 1968 *Einführung in die Metallkunde* vol 1 (Mannheim: Wissenschaftsverlag Mannheim)
[31] Huber E and Hofmann S 1994 *Surf. Coating Technol.* **68/69** 64